Investigation of the properties influencing the deactivation of iron electrodes in iron-air batteries

Nicolás I. Villanueva-Martínez [a], Cinthia Alegre [a,*], Javier Rubín [b,c], Rachel Mckerracher [d], Carlos Ponce de León [d], Horacio Antonio Figueredo Rodríguez [e], María Jesús Lázaro [a,*]

[a] *Instituto de Carboquímica, Consejo Superior de Investigaciones Científicas. C/. Miguel Luesma Castán, 4, Zaragoza 50018, Spain*
[b] *Instituto de Nanociencia y Materiales de Aragón (INMA), CSIC-Universidad de Zaragoza, Zaragoza 50009, Spain*
[c] *Departamento de Ciencia y Tecnología de Materiales y Fluidos, Universidad de Zaragoza, Zaragoza 50018, Spain*
[d] *Electrochemical Engineering Laboratory, Energy Technology Research Group, Faculty of Engineering and Physical Sciences, University of Southampton, Highfield Campus, University Road, Southampton SO17 1BJ, United Kingdom*
[e] *Escuela de Ingeniería y Ciencias, Tecnológico de Monterrey, Campus Ciudad de México, Tlalpan, Ciudad de México 14380, Mexico*
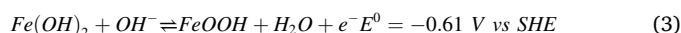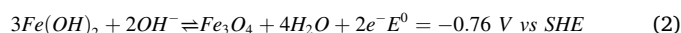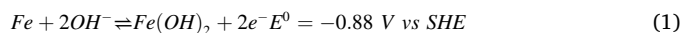
A B S T R A C T

Iron-air batteries hold the potential to be a key technology for energy storage, thanks to their energy density, low cost, safety and abundance of their materials. In order to scale the technology up and optimize the cell formulations, it is key to obtain a clear understanding of how the physical-chemical properties of the electrode influence their electrochemical behaviour, in particular, the capacity loss. In this work, we propose for the first time mathematical correlations between textural and crystallographic properties of iron electrodes and their electrochemical stability. By adjusting synthesis parameters, we were able to tune pore size and volume, surface area and crystal size of iron oxides, and found that stability is highly correlated to both surface area and pore size. Large surface area and small average pore size provide electrodes with enhanced stability. We hypothesize that the cause for deactivation is the passivation of the electrodes ascribed to the formation of a non-conductive, non-reactive iron (II) hydroxide layer during discharge, which then cannot be reduced to iron again. We validate this hypothesis with electrochemical impedance spectroscopy studies, which show that, in the more stable electrodes, the charge transfer resistance in the $Fe(OH)_2$ to Fe reduction does not significantly change after cycling, contrary to the behaviour of the less stable electrodes, corroborating our hypothesis. Furthermore, the electrode with the best properties was cycled 100 times, retaining almost 75% of its initial capacity at the end of the 100 cycles. These results are highly relevant for the future design and operation of iron-air batteries.

1. Introduction

Metal-air batteries (MABs) have gained traction in recent years due to their advantages like high theoretical energy density and specific energy, which make them suitable candidates for applications such as renewable electricity storage and electro-mobility. MABs are systems that comprise a negative electrode, where a metal (Li, Al, Zn, Fe, etc.) oxidizes, and a positive air electrode, where ambient oxygen reduces [1–3].

One type of MABs is the iron-air battery (FAB, from Fe-air battery). Its properties include 1229 Wh kg_{Fe}^{-1} of theoretical specific energy and 1273 Ah kg_{Fe}^{-1} of theoretical discharge capacity, low cost (less than 100 € kWh^{-1}), open circuit potential of 1.28 V and a high volumetric energy

density of 2500 Wh L^{-1} [4]. Other interesting properties of FABs are the use of aqueous low-cost electrolyte – generally concentrated KOH – and the safety, abundance and recyclability of iron [5]. Eqs. (1)–(3) show the half-reactions occurring during the discharge of the negative iron electrode:

$$Fe + 2OH^- \rightleftharpoons Fe(OH)_2 + 2e^-\ E^0 = -0.88\ V\ vs\ SHE \tag{1}$$

$$3Fe(OH)_2 + 2OH^- \rightleftharpoons Fe_3O_4 + 4H_2O + 2e^-\ E^0 = -0.76\ V\ vs\ SHE \tag{2}$$

$$Fe(OH)_2 + OH^- \rightleftharpoons FeOOH + H_2O + e^-\ E^0 = -0.61\ V\ vs\ SHE \tag{3}$$

Reaction 1 is the first discharge step, which is usually preferred for technological applications due to its lower equilibrium potential and

---

* Corresponding authors.
E-mail addresses: cinthia@icb.csic.es (C. Alegre), mlazaro@icb.csic.es (M.J. Lázaro).

higher number of electrodes per atom of iron involved [4]. Reactions 2–3 involve a deeper discharge of the electrode and provide less capacity and voltage. Especially, Eq. (3) provides a much lower full-cell voltage and some authors have mentioned that these deep discharges can cause damage to the electrode [6]. Even though major advances and breakthroughs have taken place in the research of FABs, two fundamental issues of the alkaline iron electrode have not been fully overcome: the low efficiency and the loss of capacity of the electrode upon cycling, also referred as deactivation, term that will be used in this work.

It has been well established that the parasitic hydrogen evolution reaction (HER) is the major cause of coulombic efficiency loss [7,8]. Together with reaction 1, HER can occur, since its standard reduction potential is less negative than the one of iron (II) hydroxide reduction, as shown in Eq. (4).

$$2H_2O + 2e^- \rightleftharpoons H_2 + 2OH^- \quad E^0 = -0.83 \; V \; vs \; SHE \tag{4}$$
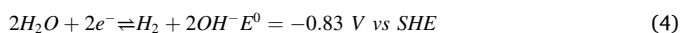
On the other hand, there is no consensus concerning the causes for deactivation and the physical-chemical properties of the electrode affecting it. Two main hypotheses have been presented to explain the loss of capacity of the iron electrode upon cycling, both of them related to the discharge products of the reactions Eqs. (1)–((3). The first one is called passivation, which is the formation of a non-conductive, non-reactive layer. The electrical conductivities of metallic iron and magnetite are around $10^7 \; \Omega^{-1} \; m^{-1}$ and $10^6 \; \Omega^{-1} \; m^{-1}$, respectively [9], however, iron (III) oxide and iron (II) hydroxide, have a much lower electrical conductivity, 7 to 8 orders of magnitude lower [10]. Passivation ascribed to a $Fe(OH)_2$ layer is the most cited explanation for the phenomenon of the deactivation of iron alkaline electrodes [11–22]. Some authors have pointed out that iron (III) oxides or hydroxides formed in the second discharge step – especially maghemite, γ-Fe_2O_3 –form a non-reactive layer [8,23,24].

The second hypothesis to explain deactivation is the molar volume increase that takes place upon oxidation of iron. When iron oxidizes to iron (II) hydroxide, it increases its molar volume up to a 272% [25]. In order to achieve a high utilization of the surface of the electrode, the former must present a large porosity, since the expansion of the iron can block those pores and prevent the electrolyte from reaching active sites [26]. Bryant et al. [27] and Yang et al. [18] calculated, based on the expansion datum, that an iron electrode should have a porosity of no less than 73% in order to be able to achieve the maximum theoretical capacity. The possibility must also not be disregarded that both molar expansion and passivation are responsible for iron electrode deactivation. Yang et al. for instance, mention an insulating layer of iron (II) hydroxide, formed after the first discharge step, that cannot be oxidized to Fe(III) and support their theory with SEM images, but they do not dismiss the effect of the porosity and the blocking effect of the molar expansion [18]. Moreover, they explain the limit of their electrodes' capacity with their lack of porosity.

Despite the major advances on electrode formulations (such as the use of additives like iron sulphide [23,24,28,29], bismuth sulphide [30, 31], bismuth oxide [32] or potassium carbonate [24,33]), to the best of our knowledge, there are no mathematical correlations able to predict the stability or capacity of iron electrodes based on their physical-chemical properties. Correlating physical-chemical properties of the electrodes to their electrochemical performance is fundamental for the rational understanding and design of efficient, cost-effective batteries. Moreover, despite several studies rely on physical-chemical characterizations of the electrodes to assert one cause or another for the electrode deactivation, no electrochemical impedance spectroscopy (EIS) studies have been carried out to investigate how the charge transfer resistance or pore diffusion resistance change over time on a single porous iron electrode. We have found in the literature one study applying EIS to assess the charge transfer resistance in porous iron electrodes. Lei et al. [34] performed EIS studies over a Ni-Fe battery after more than 100 cycles and found that the charge transfer resistance

in the iron electrode could increase up to tenfold, due to the morphological changes in the electrode.

In a previous work [35], we demonstrated that sulphur-modified iron oxides present an enhanced stability, mainly because of sulphate reduction forming sulphide, increasing conductivity. Here we evaluate the mechanisms behind the deactivation of sulphur-modified iron oxides by EIS studies. Besides, to tackle the deactivation due to the molar expansion, porous iron oxides were obtained. Mathematical correlations between their textural and crystallographic properties and their discharge capacity and stability are proposed. This work also evaluates how the charge transfer resistance changes upon cycling, indicating the causes for the electrode deactivation.

2. Experimental

2.1. Materials and methods

Porous iron oxides were synthesized according to a method established by Li et al. [36]. Since in a previous work the modification with sulphur of iron oxides proved to be effective to enhance the stability of iron electrodes, porous iron oxides were modified with sulphur by adding sodium thiosulphate in the initial mixture. 0.02 mol of tartaric acid (99.5% Labkem) plus 0.02 mol of iron (II) sulphate heptahydrate (Labkem) and 0.01 mol of sodium thiosulphate (99% Thermo Scientific Chemicals) were dissolved in 120 mL of deionized water (DI). Subsequently, 40 mL of a 1 M sodium hydroxide solution (99.99% Alfa-Aesar) was added drop by drop to the former solution under stirring for 15 min. The mixture was transferred to a Teflon-lined autoclave that was placed in a stove at 150 °C for 6 h. After the reaction time, a grey precipitate was obtained, subsequently vacuum-filtered and washed with 2 L of DI water to eliminate impurities. The obtained powder was dried overnight at 70 °C. Then, two different thermal treatments were carried out in order to assess its influence on the physical-chemical features of the sulphur-modified porous iron oxides. Half of the obtained powder was heat-treated in air atmosphere at 350 °C, and the other half was heat-treated in nitrogen atmosphere at 500 °C for 1 h. In both cases, a heating ramp of 4 °C min⁻¹ was employed. Non sulphur-modified iron oxides were also synthesized for the sake of comparison employing the same method, except for the addition of sodium thiosulphate to the initial mixture. Iron oxides so obtained (Fe_2O_3-TAR and S-Fe_2O_3-TAR) were also compared with an iron oxide obtained precipitating the iron precursor with sodium hydroxide (Fe_2O_3-SHX). Table 1 summarizes the relation of samples investigated.

2.2. Physical-chemical characterization

Nitrogen physisorption was employed to investigate the textural properties of the porous iron oxides. Isotherms at 76 K were acquired with a Micromeritics ASAP 2020 gas sorption system. Different models were applied to the N$_2$-isotherms to determine the surface area, pore volume, and pore size, respectively (Brunauer-Emmet-Teller, single

Table 1
Synthesis conditions of the different iron oxides.

Sample	Addition of tartaric acid	Addition of sodium thiosulphate	Annealing conditions
Fe_2O_3-TAR-air	Yes	No	Air @ 350 °C
S-Fe_2O_3-TAR-air	Yes	Yes	Air @ 350 °C
Fe_2O_3-TAR-N$_2$	Yes	No	N$_2$ @ 500 °C
S-Fe_2O_3-TAR-N$_2$	Yes	Yes	N$_2$ @ 500 °C
Fe_2O_3-SHX-air	No	No	Air @ 350 °C

point and Barret-Joyner-Halenda). X-ray photoelectron spectroscopy (XPS) studies were performed to evaluate the chemical composition of the samples, with an ESCA Plus Omicron spectrometer (Scienta Omicron) operated with a Mg (1253.6 eV) anode, a pass energy of 20 eV, dwell time of 0.5 s and 0.1 eV step. Orbitals C1s, O1s, S2p and Fe2p were scanned and deconvolution was carried out with the software CasaXPS (Casa Software Ltd, CasaXPS Version 2.3.18). All the peaks were fitted with a 70% Gauss / 30% Lorentz curve applying a Shirley-type baseline. Field-Emission Scanning Electron Microscopy (FESEM) was carried out with a Carl Zeiss MERLIN microscope to investigate the morphology of the samples. Transmission and Scanning Transmission Electron Microscopy (TEM/STEM) was carried out in a Tecnai F30 microscope operated at 300 kV belonging to the LMA Service of the University of Zaragoza. The samples were ultrasonically dispersed in ethanol for 15 min and then placed in a Cu carbon grid. The amounts of sulphur and oxygen in the samples were determined by Elemental Analysis (EA) in a Thermo Flash 1112 analyser (Thermoscientific Waltham), whereas the iron content was obtained using inductively coupled plasma atomic emission spectroscopy (ICP-AES) with a Jobin Ybon 2000 spectrometer. Powder X-ray diffraction (PXRD) patterns were collected with a Ru2500 Rigaku diffractometer with rotating anode and theta-2theta configuration and Cu-Kα radiation, in order to calculate phase fractions and crystallite sizes. Information on the software used to fit the diffractograms and the procedure to determine crystallite size is included in the Supporting Information (Section S3). Mössbauer spectroscopy (MS) data were acquired using a constant acceleration spectrometer with symmetrical waveform at room temperature. The source was 25 mCi 57Co/Rh. The spectra were analysed with WinNormos software and all isomer shift values are reported with respect to α-Fe.

2.3. Preparation of electrode samples

Iron oxides were mixed in a planetary ball mill with a commercial carbon black (Vulcan XC-72R) in a 1:1 mass ratio at 100 rpm for 1 h, using ethanol to favour the mixture of the solid phases. The Fe_2O_3/C composite so obtained was finally dried overnight at 70 °C. Subsequently, a mixture of polytetrafluoroethylene (PTFE) solution (60 wt% in H_2O) and water was added to the dry powder mixture in order to form a paste, that was sandwiched between two sheets of stainless-steel mesh (Alfa-Aesar, dimensions 2.5 cm x 7.5 cm) and hot-pressed at 140 °C for 90 s to obtain the working iron electrode. See Fig. S1 in Section S1 in the Supporting Information file for a scheme of the manufacturing of the electrode.

2.4. Electrochemical measurements

The electrochemical measurements were carried out with an Autolab potentiostat and Nova software in a conventional three electrode set-up consisting of a 150 cm^3 glass cell, at a temperature of 25 °C, flowing nitrogen to the electrolyte to avoid carbonation. The working electrode (WE) was placed in a PTFE holder facing the counter-electrode (CE), a nickel sheet, separated by 5 mm, as in previous works [35]. The reference electrode, an Hg|HgO in 1 M KOH solution, was placed between the WE and the CE. The electrolyte was a 6 M KOH solution (99.99% KOH, Alfa-Aesar). To determine the discharge capacity of our iron electrodes, chrono-potentiometries were carried out at a C-rate of 0.4 C (equivalent to *ca.* 16 mA) during charging and 0.2 C (equivalent to *ca.* 8 mA) during discharging (calculated according to the theoretical capacity of the electrode) [35]. Electrochemical impedance spectroscopies were carried out at −1.16 V *vs.* Hg|HgO, applying a sine wave of 10 mV, with frequencies from 1 kHz to 1 Hz and 10 points per decade.

3. Results and discussion

3.1. Iron oxides characterization

X-ray diffractograms reported in Fig. 1, confirmed that iron is present as iron (III) oxide, either as haematite or maghemite phase, in different proportions as presented in Table 2. Sulphur-modified oxides present some other minor contributions at 25° and 34° (see the fit differences, thin lines under each diffractogram, at the cited angles). In general, the fit of the experimental data to the proposed crystalline phases is good. No other crystalline phases could be clearly identified, which suggests that sulphur is present as an amorphous phase or adsorbed over the surface.

Treatment temperature and the presence of sulphur had a strong influence on both crystal phase distributions and average crystal sizes. Samples calcined in air, Fe_2O_3-TAR-air and S-Fe_2O_3-TAR-air, are composed by 80% and 65% of haematite, respectively, which is expected, since haematite is the most stable iron (III) oxide phase at room temperature. The higher amount of maghemite in S-Fe_2O_3-TAR-air is due to the presence of sulphur, that promotes a higher yield of maghemite at the expense of haematite, as reported in previous works [35]. Besides, it has been reported that impurities in iron oxides, such as sulphur, promote defects, and in fact, maghemite can be modelled as a defective iron oxide. Nitrogen-annealed samples show the opposite trend, with Fe_2O_3-TAR-N_2 and S-Fe_2O_3-TAR-N_2 having a majority of maghemite, 86% and 80%, respectively. The reducing conditions (higher temperature and nitrogen atmosphere) promote the formation of maghemite, as this phase can be obtained by the reduction of haematite [37]. In the case of Fe_2O_3-SHX-air, the high proportion of maghemite can be explained because the precipitation of iron with sodium hydroxide produces iron (II) and (III) hydroxides (green rust), which are a precursor of maghemite [38].

In all of the iron oxides, except Fe_2O_3-SHX-air, maghemite phase has an average crystal size between 9 and 10 nm, while the crystal size of haematite ranges between 12 and 24 nm (Table 2). It must be noted that crystallites of the haematite phase in Fe_2O_3-SHX-air were found to be very small, and the fit can only estimate a size below 5 nm. However, as this is the minority phase in this iron oxide, the uncertainty in the estimate does not greatly affect the average size of the said sample. S-Fe_2O_3-TAR-air has a lower crystal size than Fe_2O_3-TAR-air, explained by the defects caused by the presence of sulphur atoms, which indicates that impurities hinder the growth of Fe crystals. Li et al., found that the presence of sodium sulphate hinders the growth of haematite crystals, and seeds of Fe_2O_3 crystals were required to ensure the formation of haematite [39]. The samples annealed in nitrogen show an average crystal size around 10–11 nm, mainly due to their high maghemite content.

In an attempt to corroborate the results of X-Ray diffraction, Mössbauer spectroscopy (MS) analyses were performed (Fig. S2). Except in the sample S-Fe_2O_3-TAR-N_2, sextets corresponding to haematite and maghemite could be included in the fits and the central intensity was taken into account with a distribution of doublets. The maxima of these distributions are compatible with wüstite $Fe_{1-x}O$, oxyhydroxides [40] and hydrated iron (III) sulphates [41,42]. The higher contribution of the paramagnetic doublets in the sulphur-modified samples could indicate the presence of both oxyhydroxides and sulphates. The samples heat-treated in nitrogen atmosphere required a distribution of sextets. In the case of Fe_2O_3-TAR-N_2 this is the only component that could be included to fit the spectrum, although when a fine histogram of sextets is used a contribution of haematite is revealed, whose relative contribution has been derived by fitting the distribution above 47 T with two gaussian functions. In contrast, the spectrum of sample S-Fe_2O_3-TAR-N_2 allowed sextets for haematite and maghemite as in the samples heated in air. The need of sextets distributions in the sulphur-modified samples can be assigned to broader distributions of crystallite size including very small values, although the average sizes determined by XRD are similar to
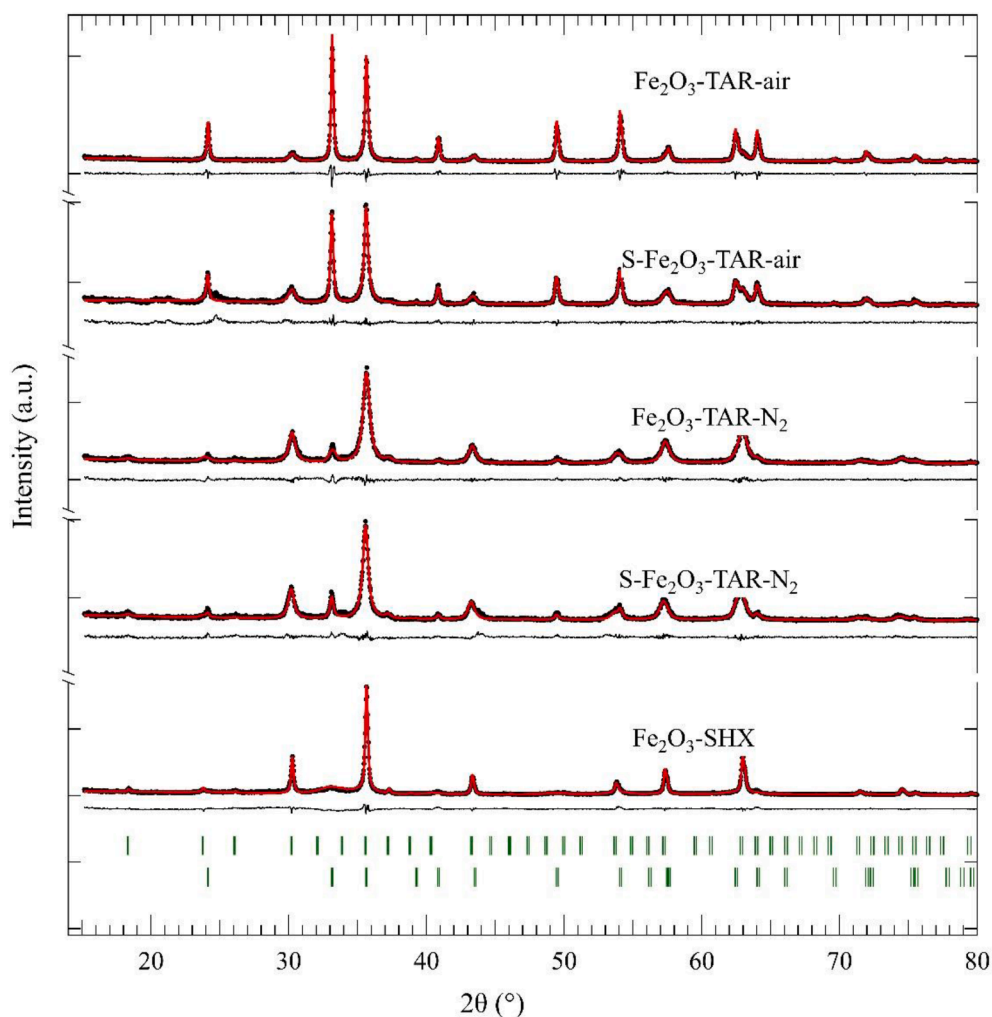
Fig. 1. Experimental X-ray diffractograms (dots), fitted profiles (thick red lines) and fit differences (thin lines). Upper row of vertical lines: maghemite reflections, lower row: haematite reflections.

Table 2
Crystal phases composition and average crystal size for the iron oxides.

Sample	Crystalline phases (%)		Crystal size (nm)		Average crystal size (nm)
	haematite	maghemite	haematite	Maghemite	
Fe$_2$O$_3$-TAR-air	80	20	24	10	21.2
S-Fe$_2$O$_3$-TAR-air	65	35	16	9	13.6
Fe$_2$O$_3$-TAR-N$_2$	14	86	12	10	10.3
S-Fe$_2$O$_3$-TAR-N$_2$	20	80	22	9	11.6
Fe$_2$O$_3$-SHX-air	15	85	4	17	15.1

Table 3
Textural properties obtained by nitrogen physisorption of the synthesized iron oxides.

Sample	Surface area (m^{2}g^{-1})	Pore volume (cm^{3}g^{-1})	Pore size (nm)	Porosity (%)
Fe$_2$O$_3$-TAR-air	141	0.30	4.8	61
S-Fe$_2$O$_3$-TAR-air	117	0.21	5.0	52
Fe$_2$O$_3$-TAR-N$_2$	28	0.10	15.9	34
S-Fe$_2$O$_3$-TAR-N$_2$	40	0.14	17.0	42
Fe$_2$O$_3$-SHX-air	77	0.17	10.3	47

those of the samples heated in air. In general, there is good agreement between XRD and MS results.

Nitrogen physisorption isotherms (Fig. S3) were carried out to investigate the textural properties of the iron oxides, reported in Table 3. Iron oxides synthesized with tartaric acid and calcined in air show type-IV isotherms, ascribed to mesoporous materials, with an hysteresis loop

that could be identified as type H4, typical of mesoporous materials with pore size greater than 4 nm [43,44]. Iron oxides annealed in nitrogen exhibit a type II isotherm, which is found in solids with little porosity [45]. A slight type H3 hysteresis loop is visible, suggesting non-rigid aggregates of plate-like particles or non-filled voids between particles (which is more plausible according to SEM images, as will be discussed later).

Surface areas range between 28 and 141 m^{2}g^{-1} and pore volumes range between 0.10 and 0.30 cm^3 g^{-1}. Both iron oxides synthesized upon tartaric acid precipitation and calcination in air at low temperature

(Fe$_2$O$_3$-TAR-air and S-Fe$_2$O$_3$-TAR-air) present the highest surface area and pore volume values. As has been described elsewhere [36,46], tartaric acid reacts in hot basic conditions with iron salts to form iron (II) tartrate. This organic salt burns or decomposes – depending on the heat-treatment conditions – and forms CO$_2$ bubbles, water and iron (III) oxides. The CO$_2$ bubbles generate voids in the iron oxides, which leads to pores in the structure. A large porosity of iron oxides is of interest, since it would entail a larger metal-electrolyte interface, and eventually, a larger specific capacity of the iron electrode. Previous reports in the literature using precipitation with tartaric acid have a significantly lower surface area (half) and larger pore size (threefold) using the same calcination conditions (air, 350 °C, 1 h), with the difference that, in the referenced work, the salt used for synthesis was iron (II) chloride [31].

Iron oxides annealed in nitrogen at higher temperatures (Fe$_2$O$_3$-TAR-N$_2$ and S-Fe$_2$O$_3$-TAR-N$_2$) present reduced values of surface area and pore volume. This could be due to a combination of the faster decomposition (due to the higher temperature) of the tartrate ion, collapsing the pore structure, along with the sintering of the iron particles, decreasing the surface area and pore volume of these iron oxides. Iron oxide obtained by precipitation with sodium hydroxide (Fe$_2$O$_3$-SHX-air) shows intermediate values of surface area and pore volume (77 m^{2}g^{-1} and 0.17 cm^{3}g^{-1} respectively) to the other set of samples, and a pore size around 10 nm (equivalent to a porosity percentage of 52%).

Porosity values (determined from the ratio between the pore volume and the density of the iron oxide, 5.26 g cm^{-3} [35]) range from 47 to 61% for the iron oxides calcined in air, and around 34 and 42% for those calcined in nitrogen. Iron oxides calcined in air are close to the 73% porosity calculated by Bryant et al., necessary to achieve an optimal utilization of the electrode surface and avoid pore plugging [27].

Bulk and surface chemical analyses, reported in Table 4, were conducted on the iron oxides by elemental analysis, ICP and XPS. Iron oxides present Fe contents ranging from 57 to 65 wt% (bulk), corresponding to around 20 at% in the surface. Sulphur-modified samples (S-Fe$_2$O$_3$-TAR-air, S-Fe$_2$O$_3$-TAR-N$_2$) present 3.5 and 2.1 wt% of S (bulk), respectively. S-Fe$_2$O$_3$-TAR-N$_2$ obtained after annealing in nitrogen at 500 °C has the lowest sulphur content, since sulphur decomposes (vaporizes) at 440 °C [47,48]. XPS results show that sulphur-modified iron oxides present high S-contents on the surface, in accordance to Li et al. work, reporting that sulphate ions remained adsorbed on the surface [36]. Table 4 also reveals that iron oxides obtained with tartaric acid present a negligible amount of carbon (ca. 0.2 wt%, except for S-Fe$_2$O$_3$-TAR-N$_2$ with 2.5 wt% C), meaning that tartrate ions are almost fully calcined during the thermal treatments, particularly using air. The large amount of surface oxygen in all the samples can be ascribed to residual water and to the presence of hydroxides, sulphate groups and hydrated sulphates, as described by Li et al. [36].

Figs. S4 and S5 show the results from the XPS characterization, the survey scan and the high resolution spectra for Fe2p and S2p orbitals, respectively. Fe$_2$O$_3$-TAR-air, Fe$_2$O$_3$-TAR-N$_2$ and Fe$_2$O$_3$-SHX-air only showed peaks at binding energies corresponding to Fe, O, and C. S2p region of S-Fe$_2$O$_3$-TAR-air and S-Fe$_2$O$_3$-TAR-N$_2$ shows one peak around 168.5 eV (2p$_{3/2}$) which was ascribed to sulphate ions, probably coming from the decomposition of the thiosulphate precursor upon oxidation in air at 350 °C. Fe2p spectrum, on its hand, shows three 2p$_{3/2}$ peaks at

710.7, 712.4 and 718.0 eV, which were assigned to Fe$_2$O$_3$, hydrated iron sulphates (either FeSO$_4$ or Fe$_2$(SO$_4$)$_3$) and the satellite of Fe$_2$O$_3$, respectively. The peak at 712 eV, according to [33], could be due to the presence of iron sulphate or iron sulphide (FeS), but the absence of peaks related to sulphide in the S2p spectrum allowed us to rule out the sulphide and conclude it is sulphate. The XPS spectra of O1s orbital (Fig. S6) shows two peaks, one around 530 eV ascribed to Fe$_2$O$_3$ and another peak around 531.5 eV, that could be ascribed to adsorbed oxygen or sulphate. Fig. S6 reveals there is a greater amount of adsorbed oxygen (or sulphate) in sulphur-modified iron oxides than in the non-modified oxides.

FESEM micrographs (Fig. S7 in the Supporting Information), alongside TEM/STEM images (Fig. S8) revealed the morphology of the iron oxides. Iron oxides based on tartaric acid and calcined in air (TAR-air, Figs. S7a and S7b, S8a–S8d) show a straw-like morphology, with pores and irregularities (formed during the calcination of the organic salt) that enhance their surface area, as mentioned before. This internal porosity can be also appreciated in the TEM images in Fig. S8. Iron oxides calcined in nitrogen (TAR-N$_2$, Fig. S7c and S7d) show signs of sintering due to the higher annealing temperature, with smaller particles, but more compact and close to each other. As a result, there are fewer voids and less space in between particles, which explains the lower pore volume and surface area of these materials. Fe$_2$O$_3$-SHX-air (Fig. S7e) presents a totally different morphology, consisting in more regular, smaller and platelet-like particles. These particles are close to each other, but the material appears to be less compact than the samples annealed in nitrogen.

3.2. Electrochemical characterization

The specific discharge capacity of the iron electrodes obtained from the previously described iron oxides was evaluated by means of charge-discharge cycles. Specifically, twenty charge-discharge galvanostatic cycles were performed at 0.4 C and 0.2 C rate respectively. Fig. 2a shows the charge and discharge curves for the fifth cycle of every Fe$_2$O$_3$/C composite. For a more detailed description of the oxidation/reduction processes, see Fig. S9.

Iron electrodes based on non-modified iron oxides, Fe$_2$O$_3$-TAR-air and Fe$_2$O$_3$-SHX-air, present the largest discharge capacities, *ca.* 300 mAh·g$_{Fe}^{-1}$ and 260 mAh· g$_{Fe}^{-1}$ for Fe$_2$O$_3$-TAR-N$_2$ at the 1st plateau (around 450–530 mAh·g$_{Fe}^{-1}$ total discharge capacity). On the other hand, electrodes based on sulphur-modified iron oxides, present lower values of discharge capacity, around 200 mAh·g^{-1} Fe (350–450 mAh·g$_{Fe}^{-1}$ total discharge capacity).

Fig. 2b–2d plot the maximum discharge capacity at the 1st plateau of each electrode against the different textural and crystallographic properties of the iron oxides. As previous studies have shown [49–51], the oxidation/reduction of iron to/from iron(II) hydroxide occurs through a dissolved intermediate, namely HFeO$_2^-$, which then precipitates. This means that the surface atoms dissolve and expose new atoms, so a lower surface area or pore volume does not necessarily mean that fewer atoms are able to react. However, there are trends between the physical-chemical properties and the discharge capacities, when considering sulphur-modified and non-sulphur modified iron oxides as different sets of data. The discharge capacity increases with surface area (Fig. 2b) and crystal size (Fig. 2d), and decreases with pore size (Fig. 2c). Due to the small amount of data points for each subset, nevertheless, it is not possible to establish correlations. The presence of sulphur diminishes the maximum discharge capacity by *ca.* 20–25%, what could be due to sulphur preventing the reduction of iron. As previously shown by XPS, sulphur is present mainly on the surface. In our previous article [35], we showed that sulphate requires several charge/discharge cycles before fully reducing to sulphide (iron sulphide can reduce to metallic iron and act as electroactive material). Besides this, the effect of the different sample morphology cannot be discarded. Samples obtained from sodium hydroxide (SHX) present a platelet-like shape whereas iron

Table 4
Elemental composition of the different iron oxides determined by ICP, EA and XPS.

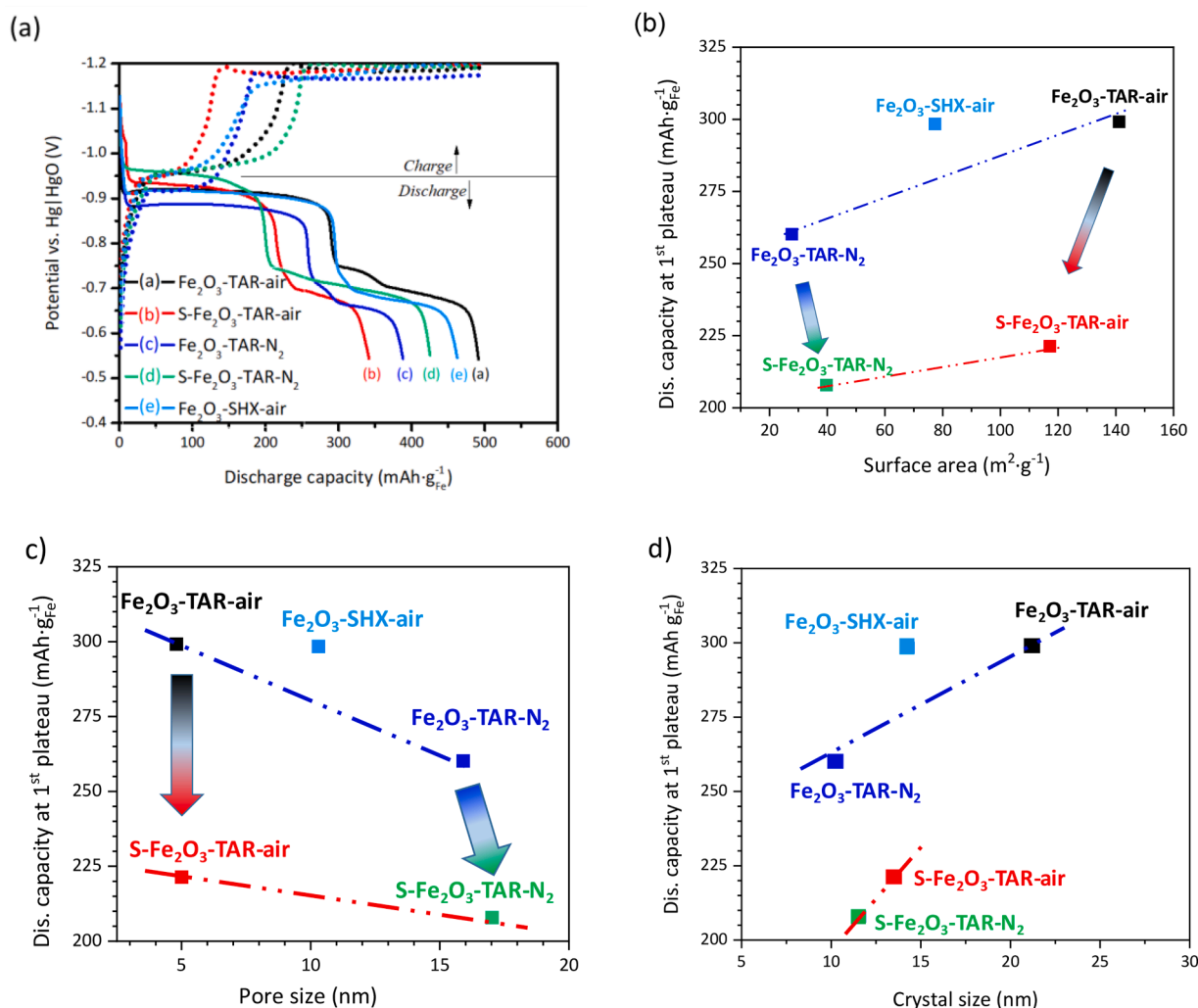| Sample	Weight% (ICP)	Weight% (EA)			Atomic% (XPS)		
	Fe	S	O	C	Fe	S	O
Fe$_2$O$_3$-TAR-air	63	–	35	0.18	22.2	–	67.1
S-Fe$_2$O$_3$-TAR-air	57	3.5	38	0.27	20.4	4.3	65.3
Fe$_2$O$_3$-TAR-N$_2$	65	–	32	0.09	19.2	–	54.4
S-Fe$_2$O$_3$-TAR-N$_2$	64	2.1	32	2.59	15.7	2.8	53.9
Fe$_2$O$_3$-SHX-air	57	–	37	–	21.8	–	66.7

Fig. 2. (a) Chronopotentiometries of the fifth cycle of each electrode and discharge capacity at the first discharge step of the different electrodes *vs.* (b) BET surface area; (c) Average pore size; and (d) average crystal size.

oxides from tartaric acid are constituted either by porous parallelepipeds (TAR-air) or spherical-agglomerates (TAR-N_2) (Fig. S7).

Fig. 3 shows a bar diagram of the maximum, average and discharge capacity at the end of the 20 charge-discharge cycles. As previously established, electrodes manufactured with Fe_2O_3-TAR-air and Fe_2O_3-SHX-air show the greatest maximum discharge capacity (more than 500 mAh·g_{Fe}^{-1} total discharge capacity) but the discharge capacity decrease by 12% and 22% after 20 cycles, respectively. On the contrary, S-Fe_2O_3-TAR-air has the lowest discharge capacity but exhibits a remarkable stability. Both samples obtained from tartaric acid calcined in air (TAR-air), show a higher stability that those calcined in nitrogen (TAR-N_2). In the case of Fe_2O_3-TAR-air, the capacity of the first discharge plateau decreases more than the one of the second (13% and 9%, respectively), which is a sign of passivation due to the formation of an insulating Fe$(OH)_2$ layer. On the other hand, Fe_2O_3-TAR-N_2 loses capacity mainly in the second discharge step (37% in the first plateau and 65%, in the second one), which means that, after Fe^0 is oxidized to Fe$(OH)_2$, it cannot be further oxidized to Fe_3O_4, FeOOH or Fe_2O_3. More evidence of this effect is found in the post-mortem XPS analysis of this electrode (Fig. S11). After full discharge, when the surface of the electrode should be completely oxidized, XPS of Fe2p region reveals that *ca.* 40% of the surface iron has 2+ oxidation state. The O1s region shows approximately that half of the surface oxygen is present as hydroxide, confirming an important coverage of iron (II) hydroxide. This could be evidence for a passivation layer formed by iron (III) oxides, but also the
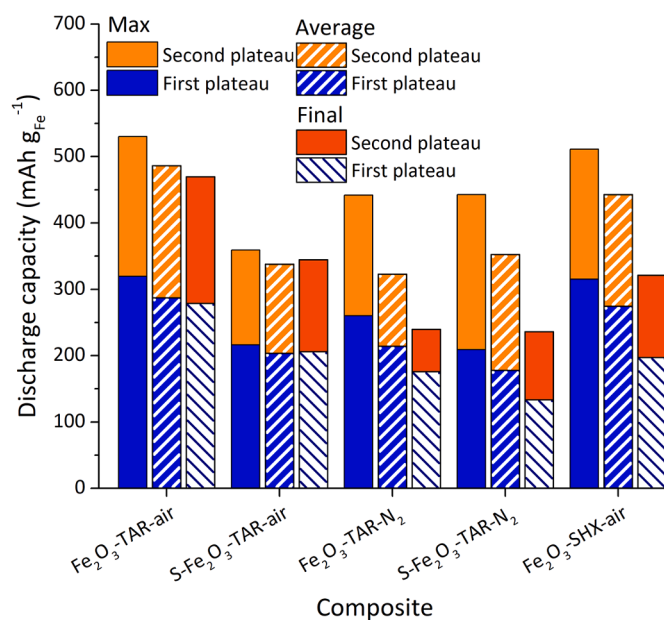

Fig. 3. Maximum, average and final discharge capacity at the 20th cycle of the iron electrodes.

explanation for this phenomenon could be found in the difference in molar volume between metallic iron and iron oxides. The expansion that comes with the oxidation, blocks the pores and prevents the electrolyte from reaching the inner iron (II) hydroxide molecules and, therefore, they cannot react and be oxidized to iron (III).

In a previous work, we established that the capacity of the electrodes slowly declines after a brief period of activation, and that the capacity of the electrodes through cycling can be described by an exponential relation [35]. Fig. 4a shows the evolution of the discharge capacity of the different electrodes during cycling. The number of activation cycles is different for each electrode, ranging from just one cycle for S-Fe$_2$O$_3$-TAR-N$_2$ to 10 for Fe$_2$O$_3$-TAR-air. In contrast, the formation of porous iron electrodes studied by Vijayamohanan et al., found that the capacity of the electrodes increases during the first cycles because the iron exposed area increases (due to dissolution and precipitation) and the electrolyte penetrates slowly in the electrode matrix [52]. Weinrich et al., also proposed that formation is partly driven by micro-structural changes in the electrode, caused by hydrogen evolution [30]. Eq. (5) models the behaviour of the electrodes upon cycling after the formation (or activation) period:

$$Q_{dis}(n) = Q_0 * f^{n-i} \tag{5}$$

where Q_{dis} (n) is the discharge capacity of a cycle n, Q_0 is the discharge capacity at the end of activation and i is the number of activation cycles. The f factor, presented for the first time in our previous work, measures the stability of each electrode [34]. An ideal electrode would have an f factor of one, meaning its capacity remains constant over time; whereas an electrode with an f factor near zero would deactivate extremely fast. Fig. 4b shows the model fitted to the data from iron oxide S-Fe$_2$O$_3$--TAR-N$_2$. Fig. S10 shows the fitting of the model to the data from the other electrodes.

Table 5 reports the f factor for each electrode, obtained by applying the model from Eq. (5) to the experimental data obtained.

Iron electrodes present stability factors above 0.95, meaning that, even the less stable material, Fe$_2$O$_3$-TAR-N$_2$, retains more than 95% of its capacity in each cycle, while S-Fe$_2$O$_3$-TAR-air, the best electrode in terms of stability, loses less than 0.2% of its discharge capacity with each cycle. The modification of the iron oxides with sulphur results in an increased stability, compensating for the loss in capacity.

The stability factor was plotted against the textural and crystallo-graphic properties of the iron oxides, to investigate the reasons behind the enhanced stability of some electrodes *versus* others (Fig. 5). Considering the R^2 values, the stability factor correlates well with surface area (Fig. 5a) and pore size (Fig. 5c), as demonstrated by the correlation coefficients of 0.87 and 0.90, respectively. It was also

Table 5
Stability factors of the manufactured electrodes.

Electrode	f factor
Fe$_2$O$_3$-TAR-air	0.989
S-Fe$_2$O$_3$-TAR-air	0.998
Fe$_2$O$_3$-TAR-N$_2$	0.953
S-Fe$_2$O$_3$-TAR-N$_2$	0.962
Fe$_2$O$_3$-SHX-air	0.975

investigated whether the textural and crystallographic properties influence the rate capability of the electrodes. For further information, see Fig. S12 in Supporting Information. Pore volume (Fig. 5b) and crystal size (Fig. 5d) do not show a high linear correlation coefficient, however, it is possible to see that there is a general trend that higher pore volume and crystal size result in a better stability. In both of them, it is the superior stability of the electrode S-Fe$_2$O$_3$-TAR-air that steers away from the lineal trend. There are three plausible hypotheses that could explain this phenomenon.

The first hypothesis is related to the molar volume change of iron species upon oxidation. A larger surface area and smaller pore size would be related to a better chance to accommodate the molecular expansion of Fe(OH)$_2$ related to metallic iron. However, if molecular expansion was the main cause for deactivation, it would be expected that the main parameter that would improve stability would be pore volume, which is not the case, as R^2 value is lower in Fig. 5b than in Fig. 5a and 5c.

The second hypothesis bases the cause of deactivation on the plugging of the pores in iron oxides, thus decreasing the active area [26]. Our evidence rules out this hypothesis, as a larger pore diameter does not correlate with a more stable electrode. Actually, the correlation is the opposite. If the clogging of the pores was the reason for the deactivation of the electrode, electrodes with bigger pore diameters would be more stable, as it is harder for larger pores to be clogged than smaller ones.

The third hypothesis relates to deactivation through passivation. Passivation occurs due to the irreversible formation of non-reactive species [8] and loss of electrical conductivity because of an isolating Fe(OH)$_2$ layer with an increased electrical resistance [52]. Both smaller pore size and larger surface area enhance the contact between iron (or iron oxides) and carbon phases. This better contact reduces electrical resistance, hence, enhancing conductivity and reactivity of the metallic oxide phase. In the case of crystal size (Fig. 5d), an insulating layer, as proposed by Figueredo-Rodríguez et al., can cover smaller crystallites more easily, and hence the positive correlation [53]. The low value of the correlation coefficient is explained by the exceptional performance of S-Fe$_2$O$_3$-TAR-air, which is caused by its textural properties and the
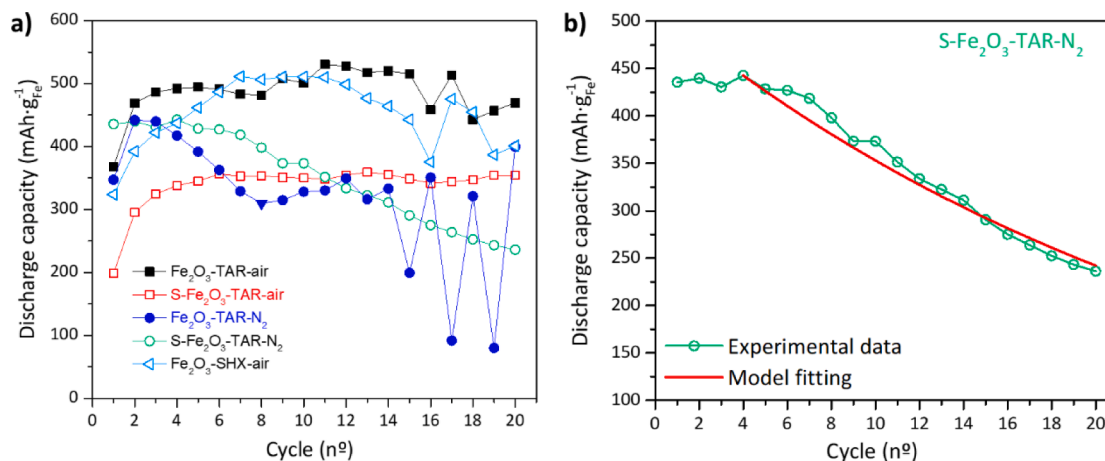

Fig. 4. (a) Discharge capacity of the electrodes along 20 charge-discharge cycles. Charge rate: 0.4 C, discharge rate: 0.2 C. (b) Comparison between the experimental data and the model from Eq. (5) for the electrode S-Fe$_2$O$_3$-TAR-N$_2$.
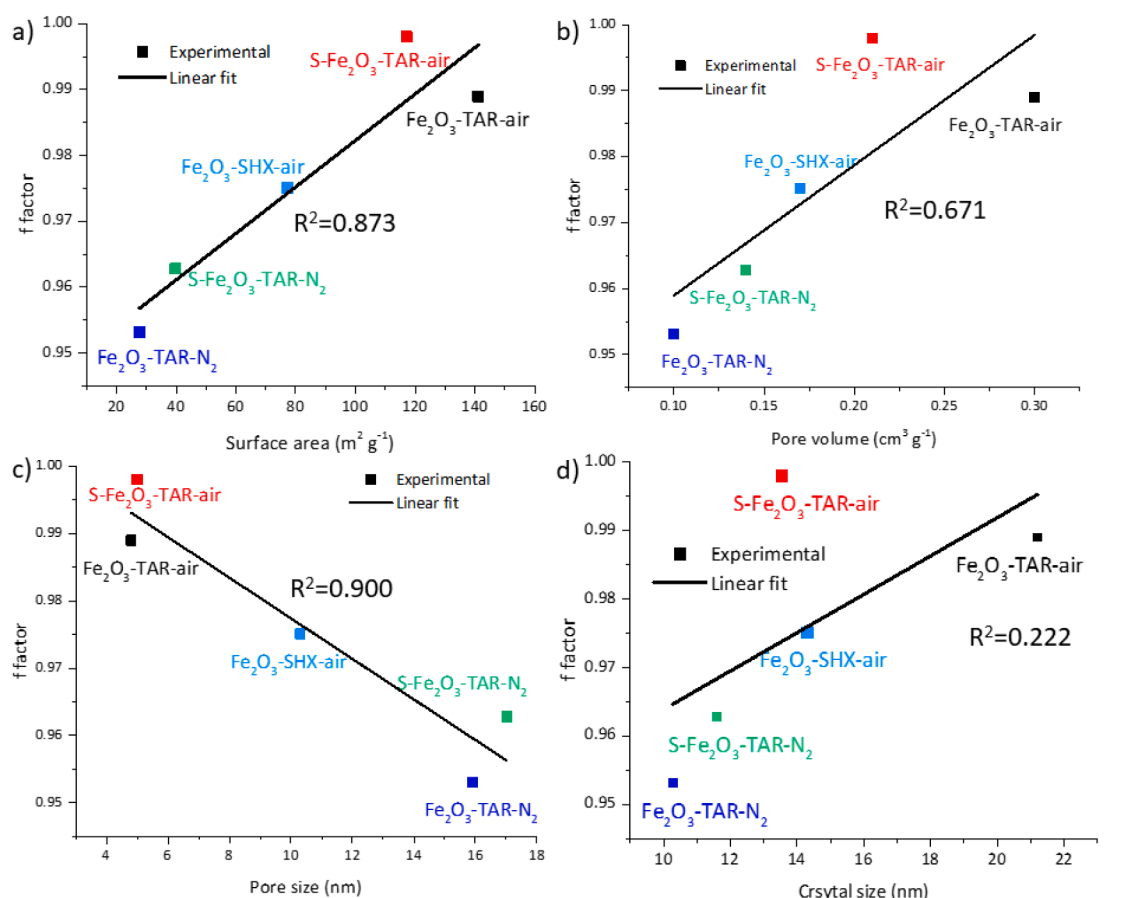
Fig. 5. Stability factors of the different electrodes *vs.* (a) Surface area; (b) Pore volume; (c) Average pore size; and (d) Average crystal size.

presence of sulphur, as will be discussed later.

To test this last hypothesis, we performed electrochemical impedance spectroscopy (EIS) studies of the different electrodes after the first charge-discharge cycle and after 15 cycles (Figs. 6 and S13) and modelled the equivalent circuit of the different phenomena occurring during the second charge step (Eq. (1) in right-to-left direction). The Nyquist diagrams show the typical "tilted", "flattened" semicircle of an electrochemical charge transfer process in a porous electrode, followed by the straight diagonal line related to diffusion impedance – Warburg impedance [54–56]. It can be seen that the Nyquist diagrams of the

electrode S-Fe_2O_3-TAR-air (Fig. 6a) are almost identical after 1 cycle and after 15 cycles, while the diagrams of electrode S-Fe_2O_3-TAR-N_2 differ significantly before and after cycling (Fig. 6b) with the semi-circle increasing in diameter, indicating a larger charge transfer resistance.

The equivalent circuit proposed for the reaction (Fig. 7) is in accordance with what Orazem and Tribollet propose for porous electrodes [57]. First, the electrolyte resistance is considered (R1). As the electrolyte is highly concentrated, and the distance from the working to the reference electrode is minimum (< 5 mm) this resistance is low, *circa* 70 $m\Omega$.
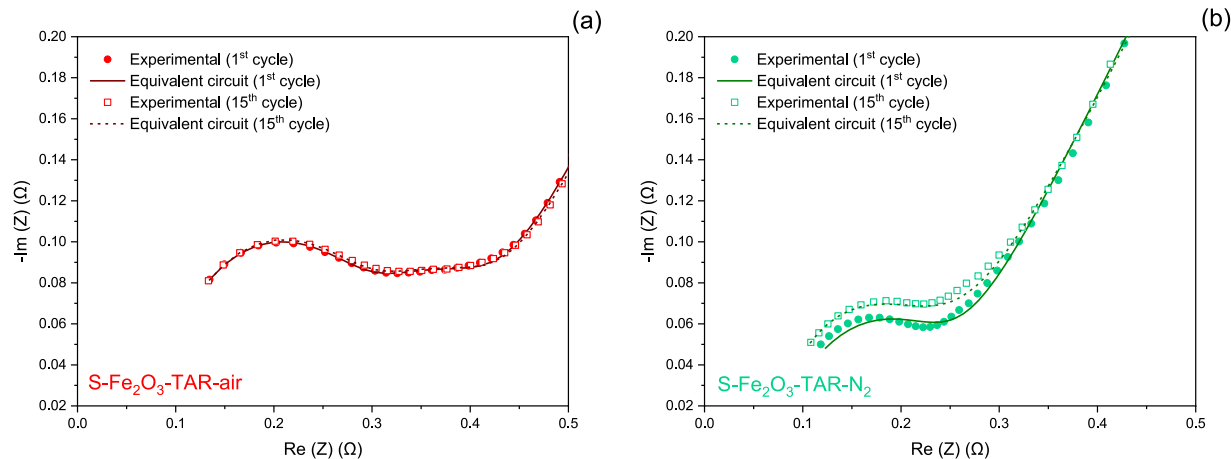

Fig. 6. Nyquist diagrams of electrochemical impedance spectroscopy studies performed at -1.16 V *vs.* Hg|HgO for electrodes: (a) S-Fe_2O_3-TAR-air and (b) S-Fe_2O_3-TAR-N_2.
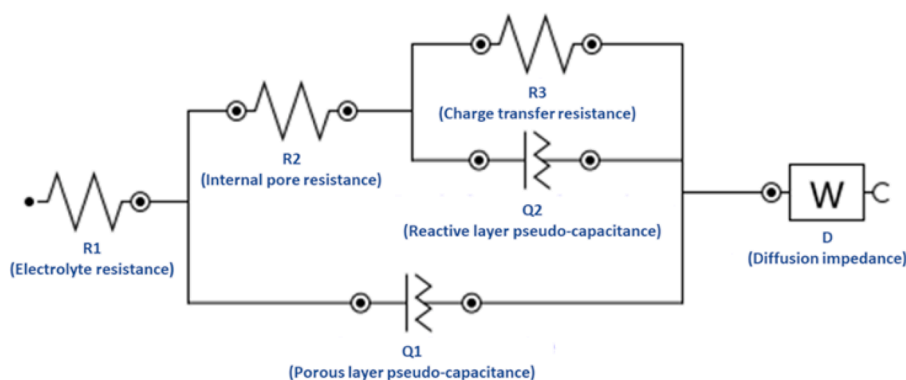
Fig. 7. Proposed equivalent circuit for the reduction of iron (II) hydroxide to iron in porous electrodes.

Then, as the concentration of the electrolyte inside the pores is not the same as in the bulk of the electrolyte, there is an electric resistance inside the pores (R2). This resistance is in parallel with the electrical double layer capacitance of the external surface of the porous layer (Q1). The internal pore resistance is in series with the charge transfer resistance (R3), which is also in parallel with the capacitance of the reactive layer (Q2). Finally, there is the impedance related to the diffusion of reactants and products from the liquid to the surface (D).

The fitted parameters (Table 6) show that, after 15 cycles, the charge transfer resistance (R3) of the electrode S-Fe$_2$O$_3$-TAR-air increases from 69.1 mΩ to 72.0 mΩ, which is only a 4.2% increment. On the other hand, in the electrode manufactured with S-Fe$_2$O$_3$-TAR-N$_2$, the charge transfer resistance (R3) increases almost sevenfold, from 18.7 to 127 mΩ. This is consistent with the stability studies, which show a much faster deactivation of the S-Fe$_2$O$_3$-TAR-N$_2$ electrode. A higher charge transfer resistance, *i.e.* a lower charge transfer admittance, is compatible with the presence of a non-conductive – and hence, non-reactive – covering layer, which is our hypothesis. In the case of S-Fe$_2$O$_3$-TAR-air, the large surface area and the small pore size entails a better contact between the carbon conductive phase and the iron hydroxide phase, thus enhancing conductivity and favoring the reduction of the iron hydroxide. In contrast, because of the lower surface area of S-Fe$_2$O$_3$-TAR-N$_2$, the iron (II) hydroxide particles have less contact with carbon, incrementing the electric resistance and being more difficult for it to reduce. Similar trends are observed in electrodes Fe$_2$O$_3$-TAR-air and Fe$_2$O$_3$-TAR-N$_2$ (Fig. S13 and Table S3 in the Supporting Information). Coincidently, sample calcined in air shows less variation in the charge transfer resistance (R3). In sample Fe$_2$O$_3$-TAR-N$_2$, the charge transfer resistance increases more than threefold, reaching 175 mV, the highest of all the samples considered.

In addition, it is possible to see that the pore diffusion resistance (R2) is considerably higher in electrode S-Fe$_2$O$_3$-TAR-air than in electrode S-Fe$_2$O$_3$-TAR-N$_2$, consistent with the fact that the oxide S-Fe$_2$O$_3$-TAR-air has 50% more porosity than S-Fe$_2$O$_3$-TAR-N$_2$ (Table 3), but S-Fe$_2$O$_3$-TAR-N$_2$ has a greater pore diameter, which means less electrolyte conduction resistance inside the pores. More evidence supporting our

deactivation hypothesis can be found in post-mortem characterizations. Electrodes S-Fe$_2$O$_3$-TAR-air and S-Fe$_2$O$_3$-TAR-N$_2$ were subjected to pre and post-cycling nitrogen physisorption experiments (see Fig. S14 in the Supporting Information).

The difference in stability between the sulphur-modified iron oxides (S-Fe$_2$O$_3$-TAR) and their non sulphur-modified (Fe$_2$O$_3$-TAR) counterparts is also compatible with the passivation due to non-conductive species. Our previous studies [35] showed that the sulphate present in the sulphur-modified iron oxides reduces to sulphide upon cycling. Sulphide has proven to prevent passivation by reacting with iron (II) hydroxide to form FeS, which is a better electric conductor than Fe(OH)$_2$ [58]. As S-Fe$_2$O$_3$-TAR-air showed the best stability upon cycling, a long run test of 130 charge-discharge cycles (more than 500 h) was performed with this electrode (Fig. 8). After 7 cycles, the electrode follows the trend of exponential deactivation as in Eq. (5), meaning the model is a good predictor of the long-term behaviour of the electrode. Aside from a few oscillations around cycles 45 and 90 – probably due to the formation of hydrogen bubbles –, the discharge capacity fits the one predicted by the model, and the overall R^2 coefficient is 0.73. The *f* factor calculated for this experiment is 0.997, which is just 0.1% lower than the one calculated for the 20 cycles experiment (shown in Fig. 4). Still, this difference means that, after 100 cycles, the electrode loses 26% of its initial discharge capacity, while the loss would have been only 18% if the long-term stability factor had been 0.998, as was calculated in the short experiment (Fig. 4).

Comparing our electrodes to others reported in literature, we could see that our electrode performs comparatively well to similar formulations. For instance, Paulraj et al. manufactured electrodes that were able to achieve 644 mAh g$_{Fe}^{-1}$ of discharge capacity and lose between 10 and 25% of it after 100 cycles, but using much more complicated formulations, including copper, tin and carbon nanotubes in the electrode and lithium hydroxide in the electrolyte [20]. Other studies focus on shorter cycling, not reaching more than 30 cycles, and showing a less stable behaviour than our electrode [33,59–62]. Other works reporting hundreds of cycles (up to 1200) are based on carbonyl iron, which has shown to be able to retain its capacity for even a few hundred cycles [13, 14,18], but with capacities of no more than 300 mAh g$_{Fe}^{-1}$ and always with the addition to the electrode or electrolyte of substances such as bismuth sulphide, sodium sulphide and bismuth oxide. Besides, carbonyl iron requires long activation periods, of even more than a hundred cycles. The only electrode found in literature based on carbonyl iron with a short activation period (25 cycles) and high discharge capacity (up to 650 mAh g$_{Fe}^{-1}$) is the one manufactured by Figueredo-Rodríguez et al. [53], who only tested 40 cycles. These results place our electrode as an interesting, low-cost, well performing alternative.

4. Conclusions

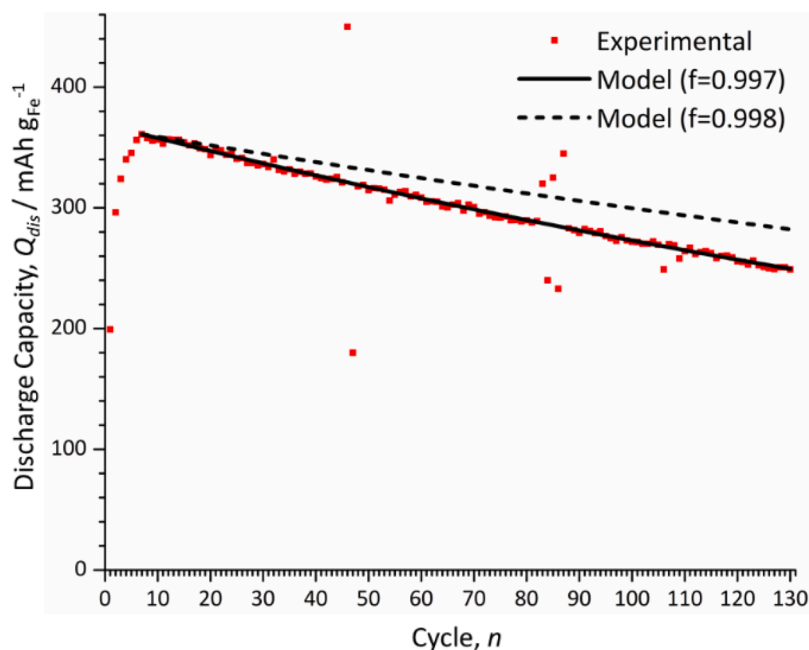Iron electrodes were manufactured based on mesoporous sulphur-

Table 6
Optimized parameters of equivalent circuit (Fig. 7) for the shown electrodes.

Electrode	S-Fe$_2$O$_3$-TAR-air		S-Fe$_2$O$_3$-TAR-N$_2$	
	1 cycle	15 cycles	1 cycle	15 cycles
R1 (mΩ)	67.5	69.2	71.0	71.3
R2 (mΩ)	239	239	159	47.1
R3 (mΩ)	69.1	72.0	18.7	127
Q1 – Y$_0$ (mS^n)	6.09	5.91	28.4	2.13
Q1 – n	0.823	0.830	0.693	0.998
Q2 – Y$_0$ (mS^n)	149	153	720	176
Q2 – n	0.887	0.887	0.692	0.513
D – Y$_0$ (S$^{0.5}$)	1.68	1.70	1.13	1.13

Fig. 8. Extended cycling of the S-Fe$_2$O$_3$-TAR-air electrode.

modified iron oxide and commercial carbon black. The physical-chemical features of the iron oxides, especially the textural properties, were tuned upon changing the synthesis conditions. We determined that textural properties, especially surface area and pore size, affect the discharge capacity of the iron oxides. More importantly, these properties have a significant impact on the stability of the electrodes. A large surface area and small pore size were linearly correlated with enhanced stability, because a good contact between the iron oxide and carbon phases was found to be crucial to prevent passivation. Electrochemical impedance spectroscopy studies evidenced that passivation is caused by a non-conductive iron (II) hydroxide layer that inhibits the reduction of this species to metallic iron. The charge transfer resistance in the Fe (OH)$_2$ to Fe reduction increases significantly in the fast-deactivating electrodes. Sulphur-modification was found to have a similar effect as the combination of using an electrode with large surface area and good contact with the carbon phase, as sulphate reduces to sulphide and forms iron (II) sulphide, which replaces iron (II) hydroxide and has a greater conductivity. Our most porous sulphur-doped iron oxide was able to run 130 cycles losing 0.3% of its discharge capacity with each cycle. All these findings provide key insights into both the deactivation mechanism and the physical-chemical properties that could prevent it, advancing one step forward the optimization and design of alkaline iron electrodes.

CRediT authorship contribution statement

Nicolás I. Villanueva-Martínez: Investigation, Methodology, Data curation, Writing – original draft, Supervision, Writing – review & editing. **Cinthia Alegre:** Conceptualization, Writing – review & editing, Data curation, Writing – original draft, Supervision. **Javier Rubín:** Conceptualization, Supervision, Writing – review & editing. **Rachel Mckerracher:** Investigation, Writing – review & editing, Supervision. **Carlos Ponce de León:** Investigation, Resources, Supervision, Writing – review & editing. **Horacio Antonio Figueredo Rodríguez:** Supervision, Writing – review & editing. **María Jesús Lázaro:** Investigation, Funding acquisition, Supervision, Writing – review & editing.

Declaration of Competing Interest

The authors declare that they have no known competing financial

interests or personal relationships that could have appeared to influence the work reported in this paper.

Acknowledgements

Supplementary materials

Supplementary material associated with this article can be found, in the online version, at doi:10.1016/j.electacta.2023.142964.

References

[1] A.G. Olabi, E.T. Sayed, T. Wilberforce, A. Jamal, A.H. Alami, K. Elsaid, S.M. A. Rahman, S.K. Shah, M.A. Abdelkareem, Metal-air batteries–a review, Energies 14 (2021) 1–46, https://doi.org/10.3390/en14217373.

[2] Q. Liu, Z. Pan, E. Wang, L. An, G. Sun, Aqueous metal-air batteries: fundamentals and applications, Energy Storage Mater. 27 (2020) 478–505, https://doi.org/10.1016/j.ensm.2019.12.011.

[3] L. Wang, D. Snihirova, M. Deng, B. Vaghefinazari, W. Xu, D. Höche, S.V. Lamaka, M.L. Zheludkevich, Sustainable aqueous metal-air batteries: an insight into electrolyte system, Energy Storage Mater. 52 (2022) 573–597, https://doi.org/10.1016/j.ensm.2022.08.032.

[4] H. Weinrich, Y.E. Durmus, H. Tempel, H. Kungl, R.A. Eichel, Silicon and iron as resource-efficient anode materials for ambient-temperature metal-air batteries: a review, Materials 12 (2019) 2134, https://doi.org/10.3390/ma121321341-55 (Basel).

[5] R.D. McKerracher, C. Ponce de Leon, R.G.A. Wills, A.A. Shah, F.C. Walsh, A review of the iron-air secondary battery for energy storage, ChemPlusChem 80 (2015) 323–335, https://doi.org/10.1002/cplu.201402238.

[6] H. Weinrich, M. Gehring, H. Tempel, H. Kungl, R.A. Eichel, Impact of the charging conditions on the discharge performance of rechargeable iron-anodes for alkaline

iron air batteries, J. Appl. Electrochem 48 (2018) 451–462, https://doi.org/10.1007/s10800-018-1176-4.

[7] J.O.G. Posada, P.J. Hall, Controlling hydrogen evolution on iron electrodes, Int. J. Hydrog. Energy 41 (2016) 20807–20817, https://doi.org/10.1016/j.ijhydene.2016.04.123.

[8] D.C. Lee, D. Lei, G. Yushin, Morphology and phase changes in iron anodes affecting their capacity and stability in rechargeable alkaline batteries, ACS Energy Lett. 3 (2018) 794–801, https://doi.org/10.1021/acsenergylett.8b00063.

[9] A.B. Hrubiak, V.O. Kotsyubynsky, V.V. Moklyak, B.K. Ostafiychuk, P.I. Kolkovsky, S.V. Fedorchenko, B.I. Rachiy, The electrical conductivity and photocatalytic activity of ultrafine iron hydroxide/oxide systems, Mol. Cryst. Liq. Cryst. 670 (2018) 97–111, https://doi.org/10.1080/15421406.2018.1542070.

[10] R.M. Cornell, U. Schwertmann, Electronic, electrical and magnetic properties and colour. The Iron Oxides: Structure, Properties, Reactions, Occurences and Uses, 2nd ed., Wiley-VCH Verlag GmbH & Co. KGaA, 2003, pp. 111–137, https://doi.org/10.1002/3527602097.

[11] B.T. Hang, M. Eashira, I. Watanabe, S. Okada, J.I. Yamaki, S.H. Yoon, I. Mochida, The effect of carbon species on the properties of Fe/C composite for metal-air battery anode, J. Power Sources 143 (2005) 256–264, https://doi.org/10.1016/j.jpowsour.2004.11.044.

[12] A.S. Rajan, S. Sampath, A.K. Shukla, An *in situ* carbon-grafted alkaline iron electrode for iron-based accumulators, Energy Environ. Sci. 7 (2014) 1110–1116, https://doi.org/10.1039/c3ee42783h.

[13] H. Weinrich, J. Pleie, B. Schmid, H. Tempel, H. Kungl, R.A. Eichel, *In situ* hydrogen evolution monitoring during the electrochemical formation and cycling of pressed-plate carbonyl iron electrodes in alkaline electrolyte, Batter. Supercaps 5 (2022) 3–10, https://doi.org/10.1002/batt.202100415.

[14] A.K. Manohar, C. Yang, S.R. Narayanan, The role of sulfide additives in achieving long cycle life rechargeable iron electrodes in alkaline batteries, J. Electrochem. Soc. 162 (2015) A1864–A1872, https://doi.org/10.1149/2.0741509jes.

[15] B.T. Hang, S.H. Yoon, S. Okada, J. Ichi Yamaki, Effect of metal-sulfide additives on electrochemical properties of nano-sized Fe₂O₃-loaded carbon for Fe/air battery anodes, J. Power Sources 168 (2007) 522–532, https://doi.org/10.1016/j.jpowsour.2007.02.067.

[16] D. Mitra, A.S. Rajan, A. Irshad, S.R. Narayanan, High performance iron electrodes with metal sulfide additives, J. Electrochem. Soc. 168 (2021), 030518, https://doi.org/10.1149/1945-7111/abe9c7.

[17] A.S. Rajan, M.K. Ravikumar, K.R. Priolkar, S. Sampath, A.K. Shukla, Carbonyl-iron electrodes for rechargeable-iron batteries, Electrochem. Energy Technol. 1 (2014) 2–9, https://doi.org/10.1515/eetech-2014-0002.

[18] C. Yang, A.K. Manohar, S.R. Narayanan, A high-performance sintered iron electrode for rechargeable alkaline batteries to enable large-scale energy storage, J. Electrochem. Soc. 164 (2017) A418–A429, https://doi.org/10.1149/2.1161702jes.

[19] B.T. Hang, T. Watanabe, M. Egashira, I. Watanabe, S. Okada, J. ichi Yamaki, The effect of additives on the electrochemical properties of Fe/C composite for Fe/air battery anode, J. Power Sources 155 (2006) 461–469, https://doi.org/10.1016/j.jpowsour.2005.04.010.

[20] A.R. Paulraj, Y. Kiros, M. Chamoun, H. Svengren, D. Noréus, M. Göthelid, B. Skårman, H. Vidarsson, M.B. Johansson, Electrochemical performance and in operando charge efficiency measurements of Cu/Sn-doped nano iron electrodes, Batteries 5 (2019) 1–15, https://doi.org/10.3390/batteries5010001.

[21] P.S. Arunkumar, T. Maiyalagan, S. Kheawhom, S. Mao, Z. Jiang, Effect of carbon material additives on hydrogen evolution at rechargeable alkaline iron battery electrodes, Mater. Sci. Energy Technol. 4 (2021) 236–241, https://doi.org/10.1016/j.mset.2021.06.007.

[22] H.T. Bui, T.M. Vu, Hydrothermal preparation of Fe₂O₃ nanoparticles for Fe-air battery anodes, J. Electron. Mater. 48 (2019) 7123–7130, https://doi.org/10.1007/s11664-019-07522-x.

[23] J. Yao, Y. Liu, H. Zhang, L. Ma, T. Meng, N. Li, J. Jiang, J. Zhu, C.M. Li, Configuring optimal FeS₂@carbon nanoreactor anodes: toward insights into pyrite phase change/failure mechanism in rechargeable Ni-Fe cells, ACS Appl. Mater. Interfaces 11 (2019) 42032–42041, https://doi.org/10.1021/acsami.9b12153.

[24] J.O. Gil Posada, P.J. Hall, Post-hoc comparisons among iron electrode formulations based on bismuth, bismuth sulphide, iron sulphide and potassium sulphide under strong alkaline conditions, J. Power Sources 268 (2014) 810–815, https://doi.org/10.1016/j.jpowsour.2014.06.126.

[25] B.E. Poling, G.H. Thomson, D.G. Friend, R.L. Rowley, W.V. Wilding, Physical and chemical data, in: D.W. Green (Ed.), Perry's Chemical Engineers' Handbook, 8th ed., McGraw-Hill, 2008 https://doi.org/10.1036/0071511253.

[26] T. Um, S.K. Wilke, H. Choe, D.C. Dunand, Effects of pore morphology on the cyclical oxidation/reduction of iron foams created via camphene-based freeze casting, J. Alloy. Compd. 845 (2020), 156278, https://doi.org/10.1016/j.jallcom.2020.156278.

[27] W.A. Bryant, The importance of physical structure to the capacity of porous iron electrodes, J. Electrochem. Soc. 126 (1979) 1899–1901, https://doi.org/10.1149/1.2128822.

[28] T.S. Balasubramanian, A.K. Shukla, Effect of metal-sulfide additives on charge/discharge reactions of the alkaline iron electrode, J. Power Sources 41 (1993) 99–105, https://doi.org/10.1016/0378-7753(93)85008-C.

[29] J.O.G. Posada, P.J. Hall, Towards the development of safe and commercially viable nickel–iron batteries: improvements to Coulombic efficiency at high iron sulphide electrode formulations, J. Appl. Electrochem. 46 (2016) 451–458, https://doi.org/10.1007/s10800-015-0911-3.

[30] H. Weinrich, M. Gehring, H. Tempel, H. Kungl, R.A. Eichel, Electrode thickness-dependent formation of porous iron electrodes for secondary alkaline iron-air

batteries, Electrochim. Acta 314 (2019) 61–71, https://doi.org/10.1016/j.electacta.2019.05.025.

[31] H. Weinrich, M. Gehring, H. Tempel, H. Kungl, R.A. Eichel, Impact of the charging conditions on the discharge performance of rechargeable iron-anodes for alkaline iron–air batteries, J. Appl. Electrochem. 48 (2018) 451–462, https://doi.org/10.1007/s10800-018-1176-4.

[32] A.K. Manohar, C. Yang, S. Malkhandi, G.K.S. Prakash, S.R. Narayanan, Enhancing the performance of the rechargeable iron electrode in alkaline batteries with bismuth oxide and iron sulfide additives, J. Electrochem. Soc. 160 (2013) A2078–A2084, https://doi.org/10.1149/2.066311jes.

[33] A.K. Manohar, S. Malkhandi, B. Yang, C. Yang, G.K. Surya Prakash, S. R. Narayanan, A high-performance rechargeable iron electrode for large-scale battery-based energy storage, J. Electrochem. Soc. 159 (2012) A1209–A1214, https://doi.org/10.1149/2.034208jes.

[34] D. Lei, D.C. Lee, E. Zhao, A. Magasinski, H.R. Jung, G. Berdichevsky, D. Steingart, G. Yushin, Iron oxide nanoconfined in carbon nanopores as high capacity anode for rechargeable alkaline batteries, Nano Energy 48 (2018) 170–179, https://doi.org/10.1016/j.nanoen.2018.03.035.

[35] N. Villanueva, C. Alegre, J. Rubin, H.A. Figueredo-Rodríguez, R.D. McKerracher, C. Ponce De León, M.J. Lázaro, Iron electrodes based on sulfur-modified iron oxides with enhanced stability for iron-air batteries, ACS Appl. Energy Mater. 5 (2022) 13439–13451, https://doi.org/10.1021/acsaem.2c02123.

[36] K. Li, Y. Zhao, M.J. Janik, C. Song, X. Guo, Facile preparation of magnetic mesoporous Fe₃O₄/C/Cu composites as high performance Fenton-like catalysts, Appl. Surf. Sci. 396 (2017) 1383–1392, https://doi.org/10.1016/j.apsusc.2016.11.170.

[37] A. Aharoni, E.H. Frei, M. Schieber, Some properties of γ-Fe₂O₃ obtained by hydrogen reduction of α-Fe₂O₃, J. Phys. Chem. Solids 23 (1962) 545–554, https://doi.org/10.1016/0022-3697(62)90512-7.

[38] R.M. Taylor, Maghemite in soils and its origin II. Maghemite syntheses at ambient temperature and pH 7, Clay Miner. 10 (1974) 299–310, https://doi.org/10.1180/claymin.1974.010.4.08.

[39] C. Li, Z. Deng, C. Wei, G. Fan, X. Li, M. Li, Y. Wang, Production of low-sulfur hematite by hydrothermal oxydrolysis of ferrous sulfate, Hydrometallurgy 178 (2018) 294–300, https://doi.org/10.1016/j.hydromet.2018.05.012.

[40] N.N. Greenwood, T.C. Gibb, Mössbauer Spectroscopy, Chapman and Hall Ltd., London, 1971.

[41] J. Gust, J. Suwalski, Use of Mössbauer spectroscopy to study reaction products of polyphenols and iron compounds, Corrosion 50 (1994) 355–365.

[42] J. de Oñate Martínez, C.D. Aguila, J.F. Bertrán, E.R. Ruíz, C.P. Vergara, R. R. Malherbe, Tribochemical reactions of erionite and Na-LTA zeolites with Fe2 (SO4) 3.5 H2O: a mössbauer study, Hyperfine Interact. 73 (1992) 371–375.

[43] J. Rouquerol, F. Rouquerol, P. Llewellyn, G. Maurin, K.S.W. Sing, Adsorption by Powders and Porous Solids: Principles, Methodology and Applications, Academic Press, 2013.

[44] S. Lowell, J.E. Shields, M.A. Thomas, M. Thommes, Characterization of Porous Solids and Powders: Surface Area, Pore Size and Density, Springer Science & Business Media, 2006.

[45] M. Thommes, K. Kaneko, A.V. Neimark, J.P. Olivier, F. Rodriguez-Reinoso, J. Rouquerol, K.S.W. Sing, Physisorption of gases, with special reference to the evaluation of surface area and pore size distribution (IUPAC Technical Report), Pure Appl. Chem. 87 (2015) 1051–1069, https://doi.org/10.1515/pac-2014-1117.

[46] J. Du, J. Bao, X. Fu, C. Lu, S.H. Kim, Mesoporous sulfur-modified iron oxide as an effective Fenton-like catalyst for degradation of bisphenol A, Appl. Catal. B Environ. 184 (2016) 132–141, https://doi.org/10.1016/j.apcatb.2015.11.015.

[47] B. Meyer, Elemental sulfur, Chem. Rev. 76 (1976) 367–388, https://doi.org/10.1021/cr60301a003.

[48] B. McDonald, J. Rice, J. Stewart, Decomposition characteristics of an elemental sulfur doped polysulfide based ramjet fuel, Combust. Flame 176 (2017) 1–11, https://doi.org/10.1016/j.combustflame.2016.10.012.

[49] H. Weinrich, J. Come, H. Tempel, H. Kungl, R.A. Eichel, N. Balke, Understanding the nanoscale redox-behavior of iron-anodes for rechargeable iron-air batteries, Nano Energy 41 (2017) 706–716, https://doi.org/10.1016/j.nanoen.2017.10.023.

[50] B. Miiller-Ziilow, R. Lacmann, M.A. Schneeweiss, Topological aspects of iron corrosion in alkaline solution by means of scanning force microscopy (SFM), Surf. Sci. 311 (31) (1994) 153–158.

[51] D.M. Dražić, C.S. Hao, The anodic dissolution process on active iron in alkaline solutions, Electrochim. Acta 27 (1982) 1409–1415, https://doi.org/10.1016/0013-4686(82)80031-5.

[52] B.T. Hang, D.H. Thang, Effect of additives on the electrochemical properties of Fe₂O₃/C nanocomposite for Fe/air battery anode, J. Electroanal. Chem. 762 (2016) 59–65, https://doi.org/10.1016/j.jelechem.2015.12.012.

[53] H.A. Figueredo-Rodríguez, R.D. McKerracher, C. Ponce de León, F.C. Walsh, Improvement of negative electrodes for iron-air batteries: comparison of different iron compounds as active materials, J. Electrochem. Soc. 166 (2019) A107–A117, https://doi.org/10.1149/2.1071816jes.

[54] H. Nara, T. Yokoshima, T. Osaka, Technology of electrochemical impedance spectroscopy for an energy-sustainable society, Curr. Opin. Electrochem. 20 (2020) 66–77, https://doi.org/10.1016/j.coelec.2020.02.026.

[55] N. Ogihara, Y. Itou, T. Sasaki, Y. Takeuchi, Impedance spectroscopy characterization of porous electrodes under different electrode thickness using a symmetric cell for high-performance lithium-ion batteries, J. Phys. Chem. C 119 (2015) 4612–4619, https://doi.org/10.1021/jp512564f.

[56] L.M. Gassa, J.R. Vilche, M. Ebert, K. Jüttner, W.J. Lorenz, Electrochemical impedance spectroscopy on porous electrodes, J. Appl. Electrochem. 20 (1990) 677–685, https://doi.org/10.1007/BF01008882.

[57] M.E. Orazem, B. Tribollet, Chapter 9: equivalent circuit analogs. Electrochemical Impedance Spectroscopy, 2nd ed., John Wiley & Sons, Inc., Hoboken, New Jersey, 2008, pp. 154–162.

[58] Q. Wang, Y. Wang, Overcoming the limiting step of Fe_2O_3 reduction via *in situ* sulfide modification, ACS Appl. Mater. Interfaces 8 (2016) 10334–10342, https://doi.org/10.1021/acsami.6b01737.

[59] H. Kitamura, L. Zhao, B.T. Hang, S. Okada, J.I. Yamaki, Effect of binder materials on cycling performance of Fe_2O_3 electrodes in alkaline solution, J. Power Sources 208 (2012) 391–396, https://doi.org/10.1016/j.jpowsour.2012.02.051.

[60] B.T. Hang, H. Hayashi, S.H. Yoon, S. Okada, J. Ichi Yamaki, Fe_2O_3-filled carbon nanotubes as a negative electrode for an Fe-air battery, J. Power Sources 178 (2008) 393–401, https://doi.org/10.1016/j.jpowsour.2007.12.012.

[61] A. Ito, L. Zhao, S. Okada, J.I. Yamaki, Synthesis of nano-Fe_3O_4-loaded tubular carbon nanofibers and their application as negative electrodes for Fe/air batteries, J. Power Sources 196 (2011) 8154–8159, https://doi.org/10.1016/j.jpowsour.2011.05.043.

[62] B.T. Hang, T. Watanabe, M. Eashira, S. Okada, J.I. Yamaki, S. Hata, S.H. Yoon, I. Mochida, The electrochemical properties of Fe_2O_3-loaded carbon electrodes for iron-air battery anodes, J. Power Sources 150 (2005) 261–271, https://doi.org/10.1016/j.jpowsour.2005.02.028.